



Cite this: *Chem. Commun.*, 2023, **59**, 11137

Received 15th July 2023,  
Accepted 17th August 2023

DOI: 10.1039/d3cc03415a

[rsc.li/chemcomm](http://rsc.li/chemcomm)

## Stable deep-blue $\text{FAPbBr}_3$ quantum dots facilitated by amorphous metal halide matrices<sup>†</sup>

Wei Shen,<sup>‡\*</sup><sup>a</sup> Yue Qiu,<sup>‡</sup><sup>a</sup> Jiayu Jiang,<sup>a</sup> Zhihua Chen,<sup>a</sup> Yanxing He,<sup>a</sup> Hao Cui,<sup>a</sup> Lihui Liu,<sup>a</sup> Gang Cheng,<sup>id</sup><sup>b</sup> Andrey N. Aleshin<sup>c</sup> and Shufen Chen<sup>id</sup><sup>\*</sup><sup>a</sup>

**This communication describes a strategy to synthesize stable deep blue  $\text{FAPbBr}_3$  quantum dots (QDs) by constructing a matrix structure. Amorphous  $\text{Ni}^{2+}$ -based metal halide matrices can stabilize QDs from both chemical and physical factors, and  $\text{Ni}^{2+}$  doping can further enhance their structural stability due to lattice shrinking. Such deep blue QD films exhibit stable X-ray diffraction patterns and photoluminescence even after 245 days of storage.**

Lead halide perovskite nanocrystals (LHP NCs) with high photoluminescent quantum yield (PLQY), tunable colors, and high color saturation have attracted great interest in the field of lighting and display.<sup>1–6</sup> As a primary color for display, deep blue LHP NCs have suffered from serious color drift and intensity degradation, which result from the ionic migration for mixed halide systems or dimensional evolution for quantum confined systems.<sup>7,8</sup> It should be noted that the ionic migration of LHP cannot be inhibited due to its ionic nature. As a double-edged sword, the quantum confinement effect leads to the band gap of LHP blueshift to realize blue emission, while quantum-confined materials with a high surface-to-volume ratio result in high surface energy and tend to be unstable.<sup>9–11</sup> Therefore, using surface engineering to decrease surface energy is an effective way to prohibit the changes of quantum-confined LHP in structure and dimension for achieving stable deep blue LHP.<sup>12</sup>

Generally, surface engineering for LHP can be employed *via* ligand passivation or construction of the core–shell/matrix structure.<sup>13,14</sup> As is known, ligand passivation is based on

chemical adsorption.<sup>15</sup> Although ligands having strong affinity, functional groups can passivate vacancies and reduce ligand shedding, the dynamic adsorption and desorption process of ligands is a key factor to degrade the optoelectronic properties of LHP in the long term.<sup>16–20</sup> According to the properties of common quantum dots (QDs), the core–shell structure can stabilize the core from both chemical and physical factors.<sup>21</sup> Whereas, such a compact core–shell structure can hardly be achieved for LHP due to the incompatibility of the ionic LHP core and covalent shell ( $\text{ZnS}$ ,  $\text{PbS}$ , *etc.*).<sup>22–24</sup> Using ionic metal halide matrix can decrease such mismatch and lattice strain to enhance the stability of  $\text{CsPbI}_3$  QDs.<sup>25–27</sup> Therefore, the fabricated metal halide matrix has the potential to construct stable deep blue QDs.<sup>28–30</sup>

Deep blue QDs were synthesized using a ligand-assisted reprecipitation method (details in the experimental section, ESI<sup>†</sup>). As shown in Fig. 1a, increasing the feeding ratios of Ni/Pb could directly adjust the QD emission colors from green to deep blue. In order to obtain the precise Ni/Pb ratios, inductively coupled plasma mass spectrometry (ICP-MS) was employed (Table S1, ESI<sup>†</sup>), and the Ni/Pb ratio was from 0 to 7.96%. According to the UV-vis spectra (Fig. 1b), a distinct first exciton absorption peak (434 nm) was observed when introducing  $\text{Ni}^{2+}$ . Such sharp exciton absorption peaks suggest a strong quantum-confined system. When the Ni/Pb ratio was greater than 1.36%, distinct second and third exciton peaks appeared, which implied QDs with high quality. Additionally, the bulk absorption peak of  $\text{FAPbBr}_3$  (535 nm) gradually decreased with increasing Ni/Pb ratio, which suggested the decrease of green emission. We also used photoluminescent (PL) spectra to monitor such evolution (Fig. 1c). In the condition of Ni/Pb = 0.44%, multiple PL peaks at the blue region could be observed, accompanied by a blueshift of green emission. When the Ni/Pb ratio increased to 0.80%, all PL peaks shifted to the blue region. The multiple PL peaks tended to be one peak when Ni/Pb ratio was 1.36%. At last, only one PL peak at 442 nm could be obtained by further increasing the Ni/Pb ratio to 4.86% or 7.96%. Based on these PL spectra, the Commission Internationale de l'Eclairage (CIE) coordinate evolution was

<sup>a</sup> State Key Laboratory of Organic Electronics and Information Displays & Institute of Advanced Materials (IAM), Nanjing University of Posts & Telecommunications, Nanjing 210023, People's Republic of China. E-mail: iamwshen@njupt.edu.cn, iamsfchen@njupt.edu.cn

<sup>b</sup> State Key Laboratory of Synthetic Chemistry, HKU-CAS Joint Laboratory on New Materials, and Department of Chemistry, The University of Hong Kong, Pokfulam Road, Hong Kong, P. R. China

<sup>c</sup> Loffe Institute, St. Petersburg 194021, Russia

† Electronic supplementary information (ESI) available. See DOI: <https://doi.org/10.1039/d3cc03415a>

‡ W. S. and Y. Q. contributed equally to this work.

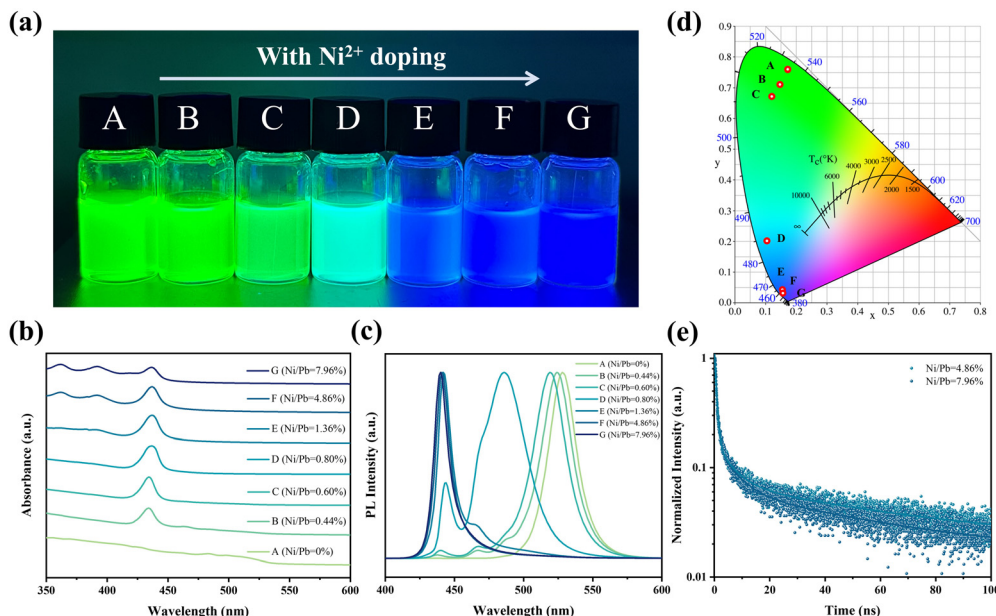


Fig. 1 (a) Images under UV-light (365 nm), (b) UV-vis absorption spectra, (c) PL spectra, and (d) CIE coordinates for  $\text{Ni}^{2+}$  doped  $\text{FAPbBr}_3$  QDs. (e) PL decay curves of deep blue QD solutions with  $\text{Ni}/\text{Pb}$  ratios of 4.86% and 7.96% (measured emission wavelength: 442 nm).

calculated (Fig. 1d), and the deep blue QDs ( $\text{Ni}/\text{Pb} = 4.8$  and 7.96%) were located at (0.058, 0.031). Furthermore, the PLQYs for both deep blue QDs were 40% and 32%, respectively, which might result in non-optically active  $\text{Ni}^{2+}$  doping. As shown in Fig. 1e and Table S2 (ESI<sup>†</sup>), the average PL lifetimes of the deep blue QDs were 62.98 ns ( $\text{Ni}/\text{Pb} = 4.86\%$ ) and 38.82 ns ( $\text{Ni}/\text{Pb} = 7.96\%$ ).

In order to study the formation mechanism of deep blue QDs, transmission electron microscopy (TEM) and high-resolution TEM (HRTEM) were employed to identify their structures. As shown in Fig. S1 (ESI<sup>†</sup>), the pristine sample ( $\text{Ni}/\text{Pb} = 0$ ) was a mixture of  $\text{FAPbBr}_3$  NCs and nanoplates. With increasing  $\text{Ni}/\text{Pb}$  ratio,  $\text{FAPbBr}_3$  NCs and nanoplates gradually decreased, and thin nanosheets appeared. Furthermore, the center of the nanosheets was not transparent, while the edge of the nanosheets showed poor crystallization, which implied the compositions of the center and edge were not the same. It should be noted that the samples exhibited a sharp deep blue emission accompanying the appearance of such nanosheets. We employed HRTEM to insight into the internal nanostructures of deep blue nanosheets ( $\text{Ni}/\text{Pb} = 4.86\%$ ). As shown in Fig. 2a, there were many black dots in the untransparent center region. Then, upon further increasing the magnification times, uniform QDs of  $2.70 \text{ nm} \pm 0.05 \text{ nm}$  (Fig. S2, ESI<sup>†</sup>) could be clearly observed (Fig. 2b), which matched well with their deep blue emission. Such QDs also exhibited good crystallization, and a clear lattice distance of 0.27 nm could be observed corresponding to the (210) plane of  $\text{FAPbBr}_3$  (the inset in Fig. 2b).<sup>31</sup> Furthermore, the compositions of nanosheets and QDs were measured by elemental mapping. A typical nanosheet (Fig. S3, ESI<sup>†</sup>) was selected with a transparent edge and an untransparent center. In a high-angle annular dark-field scanning transmission electron microscopy image (HAADF-STEM, Fig. S4a, ESI<sup>†</sup>), only the center of the nanosheet exhibited white

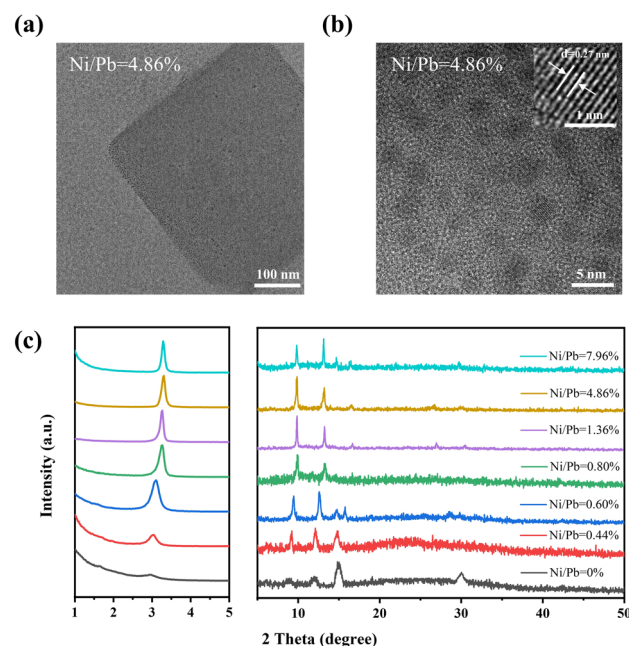


Fig. 2 HRTEM images of (a) the deep blue nanosheet and (b)  $\text{FAPbBr}_3$  QDs ( $\text{Ni}/\text{Pb} = 4.86\%$ ). Inset: Lattice distances of QDs. (c) XRD patterns of  $\text{FAPbBr}_3$  QDs ( $\text{Ni}/\text{Pb} = 0, 0.44, 0.60, 0.80, 1.36, 4.86$  and 7.96%).

color, suggesting a dense center and less dense edge. On the basis of elemental mapping images (Fig. S4b–d, ESI<sup>†</sup>), N, Pb, and Br were uniformly distributed in the center of the nanosheet. As a result, these QDs in the center were  $\text{FAPbBr}_3$  QDs. Additionally, Ni was uniformly distributed in the whole nanosheet (Fig. S4e and f, ESI<sup>†</sup>). For one part, such results suggested that  $\text{Ni}^{2+}$ -based materials were the main compositions of the nanosheet edge,

which could act as the metal halide matrix to limit the growth of  $\text{FAPbBr}_3$  QDs. As a result, small  $\text{FAPbBr}_3$  QDs could disperse uniformly and compactly in the matrix, which could prevent the dimensional evolution of QDs. In another part,  $\text{Ni}^{2+}$  might dope into  $\text{FAPbBr}_3$  QDs. The small-sized  $\text{Ni}^{2+}$  doping could induce the shrinking of the crystal lattice to enhance the stability of QDs. Then, X-ray diffraction (XRD) was employed to perform the structural characterization. As shown in Fig. 2c, two main diffraction peaks at  $15.0$  and  $30.0^\circ$  corresponded to the (100) and (200) planes, respectively, of bulk  $\text{FAPbBr}_3$ , and weak diffraction peaks at  $3.0$ ,  $8.8$ , and  $12.0^\circ$  corresponded to the characteristics of low-dimensional  $\text{FAPbBr}_3$ . According to the Bragg formula, the peak at  $3.3^\circ$  could be assigned to the size of  $2.7$  nm QDs, which matched well with the TEM results. The peaks at  $9.8$ ,  $13.1$ , and  $16.5^\circ$  were the high-order diffraction peaks of the close-packed QDs. With increasing Ni/Pb ratios, the peaks of (100) and (200) planes became weak, indicating the decrease of bulk  $\text{FAPbBr}_3$ , while the enhanced peaks of  $\text{FAPbBr}_3$  QDs confirmed an increased proportion of QDs. It should be emphasized that all the characteristics of QDs shifted to a high angle with an increasing Ni/Pb ratio. This result demonstrated that small-sized  $\text{Ni}^{2+}$  doped into  $\text{FAPbBr}_3$  QDs to replace a part of  $\text{Pb}^{2+}$ . Furthermore, we measured the XRD patterns of the  $\text{Ni}^{2+}$ -based metal halide matrix (Fig. S5, ESI<sup>†</sup>). No characteristic peaks could be obtained, which suggested that this matrix was amorphous. Therefore, such an amorphous matrix must be poor crystallinity, exhibiting no crystal lattices, and low contrast in TEM images.

Benefiting from the  $\text{Ni}^{2+}$ -based matrix and small-sized  $\text{Ni}^{2+}$  doping, the stability of deep blue  $\text{FAPbBr}_3$  QDs must be greatly enhanced. The stability of their optical properties was evaluated by accelerated aging tests, such as UV and heat aging. The UV resistance of deep blue  $\text{FAPbBr}_3$  QDs (Ni/Pb = 4.86 and 7.96%) was measured under 365 nm (8W) and 254 nm (8 W) UV lamps. PL intensity decay curves were used to identify the half-lifetimes of each sample. As shown in Fig. 3a and b, both samples exhibited stable PL spectra without the PL shift, and the PL intensities of  $\text{FAPbBr}_3$  QDs (Ni/Pb = 4.86%) degraded much more slowly. According to Fig. 3c, the half-lifetimes of each sample were 95 (Ni/Pb = 4.86%) and 28 min (Ni/Pb = 7.96%). The thermal resistance of deep blue  $\text{FAPbBr}_3$  QDs also exhibited similar results (Fig. 3d and e), and the half-lifetimes of each sample at  $60^\circ\text{C}$  were 92 (Ni/Pb = 4.86%) and 65 min (Ni/Pb = 7.96%). Therefore, a suitable Ni/Pb ratio could shrink the crystal lattice to enhance stability, while a high Ni/Pb ratio might induce more lattice distortion to decrease stability.

The structural stability of the deep-blue  $\text{FAPbBr}_3$  QDs (Ni/Pb = 4.86 and 7.96%) was also measured *via* time-dependent XRD patterns. Two deep blue films were fabricated and stored in ambient conditions. As shown in Fig. 4a,  $\text{FAPbBr}_3$  QD film (Ni/Pb = 4.86%) exhibited stable XRD patterns after 245 days of storage, and the film emitted deep blue light under a UV lamp (Fig. 4b). While the  $\text{FAPbBr}_3$  QDs film (Ni/Pb = 7.96%) exhibited much poor structural stability. Only after 35 days of storage, new XRD patterns appear accompanied by the green emission of the film. It should be noted that  $\text{Ni}^{2+}$  can

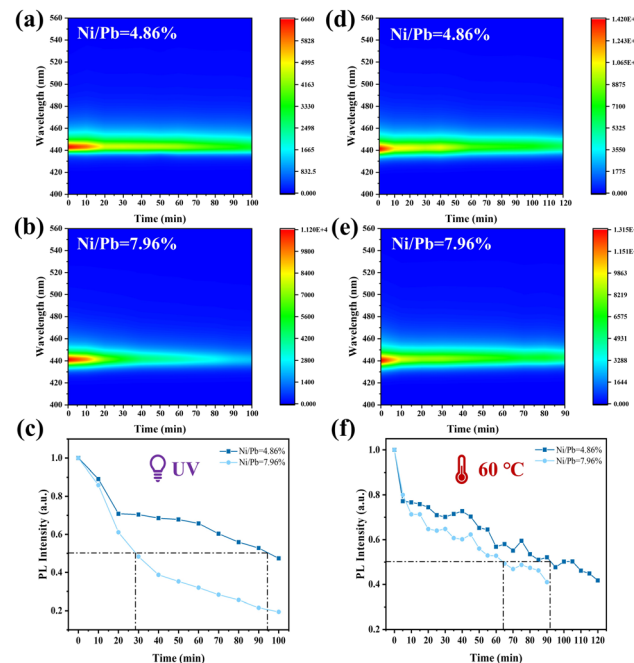


Fig. 3 The UV aging test of deep blue QD was measured under 365 nm (8W) and 254 nm (8 W) UV lamps: (a) Ni/Pb = 4.86% and (b) Ni/Pb = 7.96%. (c) PL intensity decay curves of both samples under UV irradiation. The thermal aging test of deep blue QDs at  $60^\circ\text{C}$ : (d) Ni/Pb = 4.86 and (e) Ni/Pb = 7.96%. (f) PL intensity decay curves of both samples at  $60^\circ\text{C}$ .

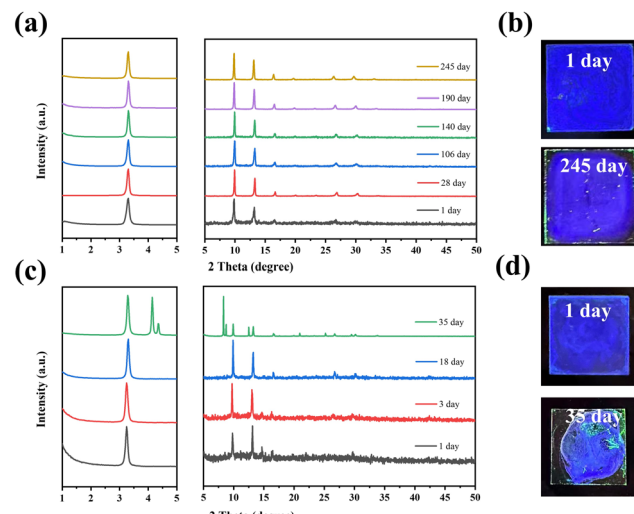


Fig. 4  $\text{FAPbBr}_3$  QDs with Ni/Pb = 4.86% thin films: (a) XRD patterns evolution, (b) images under 365 nm UV light.  $\text{FAPbBr}_3$  QDs with Ni/Pb = 7.96% thin films: (c) XRD patterns evolution, (d) images under 365 nm UV light.

easily absorb moisture. Excess  $\text{Ni}^{2+}$  will induce intense hydrolysis, resulting in poor stability. According to the above results, deep blue  $\text{FAPbBr}_3$  QDs with a 4.86% Ni/Pb ratio had the best optical and structural stabilities.

In summary, we successfully achieved stable deep blue  $\text{FAPbBr}_3$  QDs facilitated by a  $\text{Ni}^{2+}$ -based metal halide matrix.

Only if the Ni/Pb ratio was greater than 4.86%, FAPbBr<sub>3</sub> materials exhibited strong quantum confined properties, and a single PL peak at 442 nm could be obtained. Based on HRTEM and XRD results, FAPbBr<sub>3</sub> QDs were dispersed uniformly and compactly in the amorphous matrix, and a part of Ni<sup>2+</sup> was doped into FAPbBr<sub>3</sub> QDs. Benefiting from matrix protection and lattice shrinkage, FAPbBr<sub>3</sub> QDs exhibited good optical and structural stability. Therefore, the strategy of using a metal halide matrix and doping could effectively boost the stability of quantum-confined perovskite materials to realize high color saturation for lighting and display.

W. S. and Y. Q. contributed equally to this work. S. C. conceived the research. W. S. W.S. designed the experiments, analyzed data, and revised the article. Y. Q. performed the experiments and article writing. J. J. and Z. C. assisted in the stability tests. Y. X. and H. C. assisted in the tests of PLQY and PL lifetime. L. L., G. C., and N. A. assisted in article writing and revision. All authors approved the manuscript.

This work was supported by the National Natural Science Foundation of China (Grant No. 62074083, 62005131), the Priority Academic Program Development of Jiangsu Higher Education Institutions (Grant No. YX030003), the Natural Science Fund for Colleges and Universities in Jiangsu Province (Grant No. 20KJA510005).

## Conflicts of interest

There are no conflicts to declare.

## Notes and references

1. A. Dutta, R. K. Behera, P. Pal, S. Baitalik and N. Pradhan, *Angew. Chem., Int. Ed.*, 2019, **58**, 5552–5556.
2. X. Wang, Z. Bao, Y.-C. Chang and R.-S. Liu, *ACS Energy Lett.*, 2020, **5**, 3374–3396.
3. X. Zhang, C. Wang, Y. Zhang, X. Zhang, S. Wang, M. Lu, H. Cui, S. V. Kershaw, W. W. Yu and A. L. Rogach, *ACS Energy Lett.*, 2018, **4**, 242–248.
4. Y. Ji, J. B. Zhang, H. R. Shen, Z. Su, H. Cui, T. Lan, J. Q. Wang, Y. H. Chen, L. Liu, K. Cao, W. Shen and S. Chen, *ACS Omega*, 2021, **6**, 13831–13838.
5. X. Ye, C. Li, J. Jiang, X. Zheng, Q. Han, Q. Lin, Y. Liu and X. Tao, *Chem. Commun.*, 2023, **59**, 3403–3406.
6. W. Shen, J. Zhang, R. Dong, Y. Chen, L. Yang, S. Chen, Z. Su, Y. Dai, K. Cao, L. Liu, S. Chen and W. Huang, *Research*, 2021, **2021**, 9829374.
7. Z. Xiao, L. Zhao, N. L. Tran, Y. L. Lin, S. H. Silver, R. A. Kerner, N. Yao, A. Kahn, G. D. Scholes and B. P. Rand, *Nano Lett.*, 2017, **17**, 6863–6869.
8. M. Karlsson, Z. Yi, S. Reichert, X. Luo, W. Lin, Z. Zhang, C. Bao, R. Zhang, S. Bai, G. Zheng, P. Teng, L. Duan, Y. Lu, K. Zheng, T. Pullerits, C. Deibel, W. Xu, R. Friend and F. Gao, *Nat. Commun.*, 2021, **12**, 361.
9. G. Almeida, L. Goldoni, Q. Akkerman, Z. Dang, A. H. Khan, S. Marras, I. Moreels and L. Manna, *ACS Nano*, 2018, **12**, 1704–1711.
10. S. Wang, C. Bi, J. Yuan, L. Zhang and J. Tian, *ACS Energy Lett.*, 2017, **3**, 245–251.
11. C. Katan, N. Mercier and J. Even, *Chem. Rev.*, 2019, **119**, 3140–3192.
12. Y. Liu, Z. Li, J. Xu, Y. Dong, B. Chen, S. M. Park, D. Ma, S. Lee, J. E. Huang, S. Teale, O. Voznyy and E. H. Sargent, *J. Am. Chem. Soc.*, 2022, **144**, 4009–4016.
13. A. Patra, S. Bera, D. Nasipuri, S. K. Dutta and N. Pradhan, *ACS Energy Lett.*, 2021, **6**, 2682–2689.
14. Y. Zeng, W. Chen, Y. Deng, W. Gu, C. Wu, Y. Guo, P. Huang, F. Liu and H. Li, *ACS Appl. Nano Mater.*, 2022, **5**, 9534–9543.
15. W. Shen, Y. Yu, W. Zhang, Y. Chen, J. Zhang, L. Yang, J. Feng, G. Cheng, L. Liu and S. Chen, *ACS Appl. Mater. Interfaces*, 2022, **14**, 5682–5691.
16. H. Zhang, M. K. Nazeeruddin and W. C. H. Choy, *Adv. Mater.*, 2019, **31**, e1805702.
17. M. Jiang, Z. Hu, Z. Liu, Z. Wu, L. K. Ono and Y. Qi, *ACS Energy Lett.*, 2019, **4**, 2731–2738.
18. W. Shen, Z. Su, S. Chen, Y. Dai, Y. Qiu, Y. Chen, J. Jiang, J. Zhang, Y. Wang, H. Cui, Y. He, K. Cao, B. Cai, L. Liu and S. Chen, *Adv. Opt. Mater.*, 2023, 2300306.
19. W. Shen, Y. Dai, B. Cai, S. Chen, H. Yang, Y. Ma, Y. Chen, Z. Su, J. Zhang, Y. Qiu, Y. Wang, J. Jiang, L. Liu, K. Cao and S. Chen, *ACS Energy Lett.*, 2023, **8**, 2561–2569.
20. Z. Wei, K. Wang, W. Zhao, Y. Gao, Q. Hu, K. Chen and L. Dou, *Chem. Commun.*, 2021, **57**, 11469–11472.
21. Y. Wang, A. Li, Y. Hu, Y. Bao, Y. Zhang, X. Hu and N. Zhuang, *Chem. Commun.*, 2021, **57**, 1356–1359.
22. J. Zhu, L. Zhou, Y. Zhu, J. Huang, L. Hou, J. Shen, S. Dai and C. Li, *Small*, 2022, **18**, e2104399.
23. Y. Meng, Z. Lai, F. Li, W. Wang, S. Yip, Q. Quan, X. Bu, F. Wang, Y. Bao, T. Hosomi, T. Takahashi, K. Nagashima, T. Yanagida, J. Liu and J. C. Ho, *ACS Nano*, 2020, **14**, 12749–12760.
24. T. K. O. Vu, I. W. Cho, J. Oh, D. U. Lee, M. Y. Ryu and E. K. Kim, *J. Colloid Interface Sci.*, 2021, **590**, 19–27.
25. Y. Liu, Y. Dong, T. Zhu, D. Ma, A. Proppe, B. Chen, C. Zheng, Y. Hou, S. Lee, B. Sun, E. H. Jung, F. Yuan, Y. K. Wang, L. K. Sagar, S. Hoogland, F. P. Garcia de Arquer, M. J. Choi, K. Singh, S. O. Kelley, O. Voznyy, Z. H. Lu and E. H. Sargent, *J. Am. Chem. Soc.*, 2021, **143**, 15606–15615.
26. Y. Shi, L. Yuan, Z. Liu, Y. Lu, B. Yuan, W. Shen, B. Xue, Y. Zhang, Y. Qian, F. Li, X. Zhang, Y. Liu, Y. Wang, L. Wang, J. Yuan, L. S. Liao, B. Yang, Y. Yu and W. Ma, *ACS Nano*, 2022, **16**, 10534–10544.
27. X. Ling, J. Yuan, X. Zhang, Y. Qian, S. M. Zakeeruddin, B. W. Larson, Q. Zhao, J. Shi, J. Yang, K. Ji, Y. Zhang, Y. Wang, C. Zhang, S. Duhm, J. M. Luther, M. Gratzel and W. Ma, *Adv. Mater.*, 2020, **32**, e2001906.
28. L. Kong, X. Zhang, C. Zhang, L. Wang, S. Wang, F. Cao, D. Zhao, A. L. Rogach and X. Yang, *Adv. Mater.*, 2022, **34**, 2205217.
29. C. Zhang, S. Wang, X. Li, M. Yuan, L. Turyanska and X. Yang, *Adv. Funct. Mater.*, 2020, **30**, 1910582.
30. H. Wang, X. Gong, D. Zhao, Y.-B. Zhao, S. Wang, J. Zhang, L. Kong, B. Wei, R. Quintero-Bermudez, O. Voznyy, Y. Shang, Z. Ning, Y. Yan, E. H. Sargent and X. Yang, *Joule*, 2020, **4**, 1977–1987.
31. Q. Xiong, S. Huang, J. Du, X. Tang, F. Zeng, Z. Liu, Z. Zhang, T. Shi, J. Yang, D. Wu, H. Lin, Z. Luo and Y. Leng, *Adv. Opt. Mater.*, 2020, **8**, 2000977.